Extreme Mechanics Letters 54 (2022) 101739

Contents lists available at ScienceDirect

Extreme Mechanics Letters

journal homepage: www.elsevier.com/locate/eml

Doping kinetics in organic mixed ionic–electronic conductors: Moving front experiments and the stress effect

Xiaokang Wang [a], Xuefei Li [b], Jianguo Mei [b], Kejie Zhao [a,*]

[a] School of Mechanical Engineering, Purdue University, West Lafayette, IN 47907, USA
[b] Department of Chemistry, Purdue University, West Lafayette, IN 47907, USA

ARTICLE INFO

Article history:
Received 22 February 2022
Received in revised form 5 April 2022
Accepted 10 April 2022
Available online 16 April 2022

Keywords:
Doping kinetics
Organic mixed ionic–electronic conductor
Redox reaction
Stress
Diffusion

ABSTRACT

Organic mixed ionic–electronic conductors (OMIECs) are the core functional component of various organic electrochemical devices. To be highly conductive, OMIECs require electrochemical doping by electron/hole extraction and charge compensation by counter ions, which often induces concomitant changes in material properties for their electrical, optical, and mechanical behaviors. Here, we characterize the doping kinetics of a model solid-state poly(3,4-propylene dioxythiophene) (PProDOT) thin film via a designed moving front experiment using optical microscopy and in-situ nanoindentation. The in-plane front propagation displacement shows bilinear dependence on the square root of time, indicating a diffusion-controlled process. Nanoindentation results show drastic changes in the film morphology and the elastic modulus and hardness upon doping. As the swelling-induced stress may bias the doping kinetics, we observe that an applied pressure as low as 2.8 MPa significantly retards the electrochemical redox reaction. Theoretical modeling is proposed and implemented using the finite element method, which well captures the doping kinetics of PProDOT under stress. We also evaluate the diffusivity dependence on the doping level and the mechanical stress. This work sheds light on the coupled electrochemical and mechanical responses of OMIECs.

1. Introduction

Organic mixed ionic–electronic conductors are an emerging family of materials of promising applications in organic electrochemical transistors [1,2], optical modulators [3], energy harvesters/storage, and light-emitting devices [4,5]. For example, organic electrochromic materials modulate the intensity of the incoming light when integrated into smart windows and optical shutters, as shown in Fig. 1-Application. Unlike traditional inorganic-based electrochromic materials, organic electrochromic polymers often exhibit intrinsically high optical contrast ratios, fast switching speeds, and high coloration efficiencies. The excellent performance of OMIECs originates from their dual ionic and electronic conduction. Usually insulative in their neutral state, OMIECs can be doped by extracting electrons/holes under very low voltage (<1 V) for electronic conduction, which is accompanied by ion insertion/expulsion for electroneutrality [6,7]. Doping often induces (i) electronic structural changes, manifested as the electrochromic behavior [8], and (ii) phase and microstructural changes, presented as volumetric swelling and material softening [9,10].

The doping process of thin-film OMIECs is well studied in the liquid electrolyte, where the ionic transport takes place in the thickness direction and diffusion is rarely the rate-limiting process [10]. The doping kinetics in liquid electrolyte is focused ion injection [11,12], structural relaxation [13,14], and neutral–polaron–bipolaron transitions [13,15] which are typically on the subsecond time scale. Electrochemical measurements spanning longer time scales, such as cyclic voltammetry, are also employed [10,16,17]. Alongside the studies of doping kinetics in the liquid environment, solid-state doping that involves diffusion over longer time and distance offers additional insight in the switching kinetics. This is also of practical importance given that electrochemical devices are often made as solid state to limit the excessive swelling induced by solvent uptake [18,19] and for improved durability [20].

Moving front experiments present a unique way of characterizing solid-state doping kinetics of OMIECs [21]. In a typical setup, a thin-film electrode is partially covered by an ion-blocking layer. The uncovered part is immersed in a liquid electrolyte and connected with a counter electrode and a reference electrode [22]. Under an applied voltage, the OMIECs film in contact with the liquid electrolyte is doped [23]. In contrast, the region without direct contact with the electrolyte relies on the ion supply from the neighboring doped region. The redox front separating the doped and un-doped regions moves under the

* Corresponding author.
E-mail address: kjzhao@purdue.edu (K. Zhao).

https://doi.org/10.1016/j.eml.2022.101739
2352-4316/

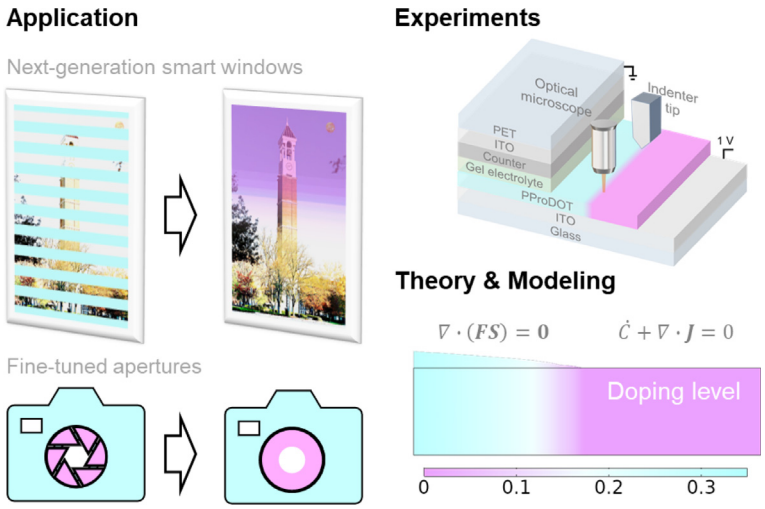

Fig. 1. Schematics of doping kinetics study using combined techniques of moving front experiments and theoretical modeling for advanced optical devices. (For interpretation of the references to color in this figure legend, the reader is referred to the web version of this article.)

thermodynamic driving force [15]. The setup has allowed the direct measurement of ion mobility [24], establishment of doping models [25], and understanding of ion transport mechanisms [26,27]. When incorporated with electrochromic technologies, the moving redox front separating the transmissive and colored regions allows active color control with enhanced temporal and spatial resolutions [28], which benefits applications including customized dynamic windows and fine-tuned aperture sizes for minimized image distortion in cameras [29], as sketched in Fig. 1-Application. Note that the above work involves the use of an ionic barrier material, which makes the mechanical testing and morphological characterization of the film difficult.

We further note that mechanical stresses may also impact the doping process. Theory and experiments show that ion insertion-induced swelling causes compressive stresses on the order of ∼10 MPa in polypyrrole thin films [9,30]. The solid-state OMIEC devices may also be subject to mechanical load or stacking pressure in their applications. Moreover, stretchable organic electronic/electrochemical devices [31] and polymer actuators [32] are inevitably under stress during operation. Mechanical stresses modify the chemical potential of the mobile species and change its transport behavior in the OMIECs [33,34]. However, the extent to which stress modifies the doping kinetics remains elusive. This knowledge gap can be bridged by considering the coupled electrochemical and mechanical responses as shown in Fig. 1-Theory.

Here, we utilize the moving front setup combined with in-situ nanoindentation to characterize the doping kinetics and its dependence on stress during redox switching in a model electrochromic OMIEC polymer, poly(3,4-propylene dioxythiophene) (PProDOT). We show that the front propagation is governed by the ion diffusional characteristic, as demonstrated by the real-time observation and finite element modeling (FEM) using the experimental data of elastic modulus, hardness, and volumetric strain across the moving front. We find that an externally applied pressure of 2.8 MPa significantly retards the propagation of the moving front, due to the stress contribution to the chemical potential and diffusivity of the mobile ions.

2. Results and discussion

We design the moving front experiment as shown in the schematic of Fig. 1-Experiments. The left portion of the setup is a full electrochromic device, consisting of stacking layers of an OMIECs thin film, a gel electrolyte for ion conduction, a counter electrode for charge balancing, and indium-tin oxide (ITO)-coated glass substrates as current collectors. This moving front setup allows the characterization of solid-state doping kinetics and mechanical properties of the PProDOT [3,35] thin film. An in-situ optical microscopy is used to observe the time evolution of the moving front. With an applied voltage of 1 V, the PProDOT film in contact with the gel electrolyte is doped with holes/anions and bleached to transmissive light blue. Then the redox carriers move towards the pristine magenta domain ahead of the moving front on the right. The microscopic images (scale bar 100 μm) in Fig. 2(a) captured at 0, 1 h, and 10 h and Video S1 show the propagation of the front. The front propagation length L is defined as the distance from the ion source to the front position as seen visually from the microscopic images. The resolution (pixel size in the microscope images) is ∼1 μm. We plot the front displacement L against the square root of time $\sqrt{t}$ in Fig. 2(b). The shaded area represents the standard deviation of the front displacement measured from three different devices. The bilinear curve in Fig. 2(b) indicates the diffusional characteristic of the front propagation. The faster kinetics in the first stage is mostly attributed to the surface diffusion of ions due to the excessive gel electrolyte covered on the film during the assembly process. The excessive coverage is formed when the counter electrode is attached on top of the liquid gel precursor before photocuring, and the liquid electrolyte flows beyond the edge of the counter electrode. Once the surface excessive ions are depleted, surface diffusion is minimized, and bulk diffusion through the doped region becomes dominant which takes more time and slows the front propagation. The transition takes place at ∼4 h after the voltage is applied. The diffusivity is calculated by $D = L^2/2t$ for one-dimensional diffusion and the results are $D_1 = 7.80 \times 10^{-12}$ m^2 s^{-1} in the first stage and $D_2 = 1.52 \times 10^{-12}$ m^2 s^{-1} afterward [36]. Using materials with proper conductivity/diffusivity can yield desired and reversible moving front in specific applications [24,37].

We utilized in-situ nanoindentation residing in a glovebox to measure the mechanical properties and swelling behavior of PProDOT thin film in liquid electrolytes in our previous work [9,10]. Combined with the moving front experiment, the doped region with an exposed surface allows in-situ mechanical characterization of the doping process in solid-state devices. The PProDOT of different redox states, separated by the moving front, show drastically different properties as measured by nanoindentation experiments. The tests are performed after ∼48 h of

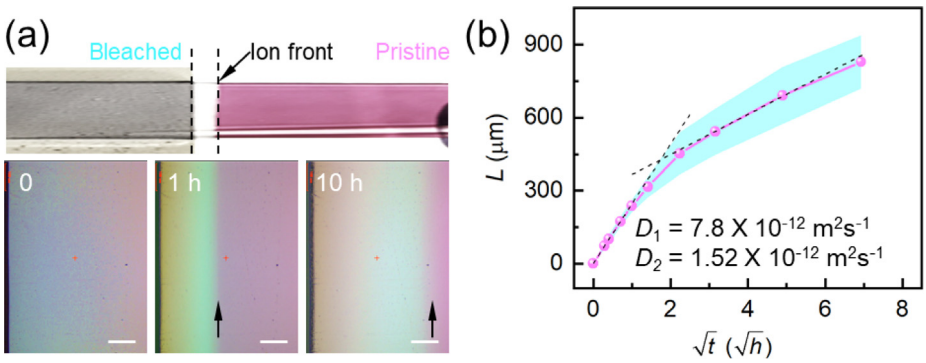

Fig. 2. Kinetics of the moving front in PProDOT thin film. (a) Camera photo (upper panel) and optical microscopic image (lower panel) at 48 h and snapshots at 0, 1 h, and 10 h of the PProDOT film under 1 V bias voltage. The moving front is indicated by arrows. The scale bar is 100 μm. (b) Moving front displacement as a function of the square root of time. Inset values are the apparent diffusivity for the two linear domains. (For interpretation of the references to color in this figure legend, the reader is referred to the web version of this article.)

front propagation in thick films (∼425 nm). At this time, the front is nearly immobile during the measurement. The load–displacement curves are recorded (Figure S1), and the substrate independent elastic modulus and hardness are calculated as shown in Fig. 3(a) and (b), where the shaded regions in cyan represent the standard deviation. Due to the ion insertion and microstructural change of the PProDOT film, the doped region behind the moving front (left to the dashed line) has drastically decreased modulus ($E = 422 \pm 100$ MPa) and hardness ($H = 33 \pm 7$ MPa) compared to the pristine magenta phase ($E = 1063 \pm 53$ MPa, $H = 78 \pm 6$ MPa) ahead of the front. The results agree with our previous work measured in the liquid environment [9]. The measured thickness of the film for the doped region shows an increase of 143 nm than the pristine region, Fig. 3(c). Since the in-plane deformation of the film is bounded by the substrate, this corresponds to a volumetric strain of $\varepsilon_V = \frac{\delta h}{h_0} = \frac{143}{425} \times 100\% = 34\%$ in PProDOT. This swelling ratio is consistent with and near the upper bound of swelling of PProDOT in the liquid environment [9,10].

The huge volumetric swelling would lead to enormous stresses in the film if one assumes an elastic response of PProDOT, and the overestimated stress may dominate the thermodynamic driving force of the doping process. We estimate the yield strength of PProDOT as the upper bound of the stress in the film upon doping. We adopt a well-used formula by Marsh [38] and others [39]. Using a Vickers indenter tip, Marsh showed that, different from FCC metals, the elastic modulus E, hardness H, and yield strength Y of a variety of materials such as steels and polymers are related via $\frac{H}{Y} = 0.28 + 0.60\frac{3}{3-A}\ln\left(\frac{3}{A+3B-AB}\right)$, where $A = (1-2\nu)\frac{Y}{E}$, $B = (1+\nu)\frac{Y}{E}$, and ν is the Poisson's ratio. With elastic modulus and hardness measured at different locations, we solve the above equation and plot the yield strength in magenta in Fig. 3(d). Clearly, doping softens the material, causing the yield strength to decrease from 35 MPa to 11 MPa from the pristine to the doped states. If material pile-up [40] occurs underneath the indenter tip, one would underestimate the contact area and thus overestimate the modulus/hardness. Using the lower limit of the measured modulus and hardness (average minus standard deviation), we plot the yield strength as if pile-up occurred in Fig. 3(d) in cyan. Similarly, we also estimate the upper bound of yield strength when material sink-in may happen during the nanoindentation experiments as shown in Fig. 3(d).

To understand the kinetics of the moving front, we consider mass transport of a single mobile species in a host undergoing large deformation and implement the theory into finite element modeling, as described in detail in Section 4 *Method*. Some important parameters are listed as follows. The charge to fully dope a thin film of the volume $V = 3\text{ cm} \times 0.7\text{ cm} \times 100\text{ nm}$ is measured as $Q = 2.78$ mC. Then the ion concentration within the doped film is $\frac{Q}{VF} = 1372$ mol m^{-3}, where F is the Faraday's constant. Here, we define the doping level C_{doping} as the ion concentration (single charged) normalized by the maximum concentration. For polymers like PProDOT, the maximum doping level is about 33% [41]. Therefore in the model, a concentration of 1372 mol m^{-3} corresponds to the doping level of 33%. The gel electrolyte is considered as an ion reservoir. Since all ions supplied to the front transport through the doped region, we treat the portion of the PProDOT in direct contact with the electrolyte as an ion source with a fixed doping level of $C_{\text{doping}} = 0.33$. To avoid singularity of the chemical potential due to the logarithm term, the minimum concentration is set as 1 mol m^{-3} at the right boundary and as the initial value for the entire model.

Once doped, the ionic diffusivity and electronic conductivity of OMIECs will increase by several orders of magnitude [42]. Aside from the contribution of pressure to the chemical potential of the mobile species, hydrostatic stress also modifies the ionic diffusivity due to the change of the free volume of the host [43–45]. These observations lead to the decomposition of the apparent diffusivity D_{app} (as shown in Fig. 2(b)) into three components, $D_{\text{app}} = f_{\text{d}} D_0 \exp\left[-f_{\text{C}}\left(C_{\text{doping}} - 0.33\right)^2\right] \exp\left(f_{\text{s}}\frac{\sigma_{\text{m}}}{G}\right)$, where D_0 is the ionic diffusivity in the pristine PProDOT free of stress and without an applied voltage, f_{d}, f_{C}, and f_{s} are constants to be determined, G is the shear modulus and is related to elastic modulus by $G = \frac{E}{2(1+\nu)}$ where $\nu = 0.3$ is the Poisson's ratio. The term $f_{\text{d}} D_0$ is determined by fitting the front propagation length. The exponential term with f_{C} accounts for the dependence of diffusivity on the doping level, which controls the widths of the front. The exponential term with f_{s} accounts for the impact of the mean stress σ_{m}, defined as $\sigma_{\text{m}} = (\sigma_x + \sigma_y + \sigma_z)/3$, on ionic diffusivity. We set $D_0 = D_{\text{app}}$ as the initial value and then adjust the parameters such that the modeling results match the experimental measurement. For the front propagation modeling, we do not consider the stress effect and thus set $f_{\text{s}} = 0$. When evaluating the stress effect on diffusivity in the later section of the work, we choose a lower limit of the stress factor in the literature [43] and set $f_{\text{s}} = 6$.

Past studies showed that a steep change in diffusivity as a function of the doping level is necessary to produce a sharp moving front [26]. To evaluate the dependence of the ionic diffusivity on the doping level, we determine the parameter f_{C} such that the front width at 2 h is the same for the experiments and modeling. In experiments, the front width (∼37 μm) is evaluated visually by optical images with calibrated scale bars, as shown in Figure S2. In modeling, we define the front width as the distance along which the doping level drops from 36% of the maximum doping level,

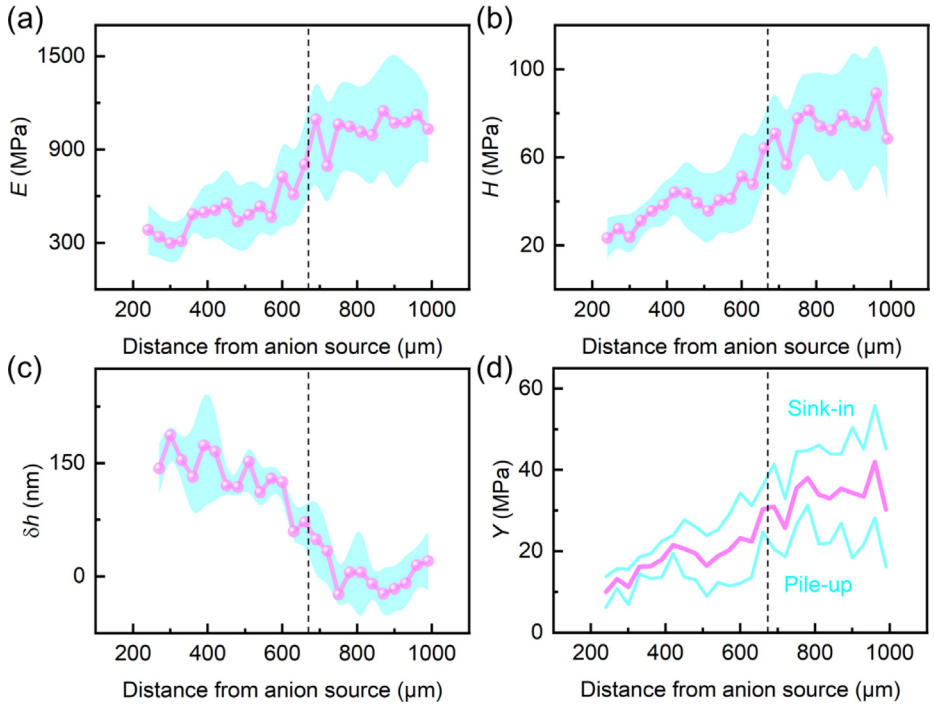

Fig. 3. Mechanical characterization of the PProDOT film near the moving front on (a) elastic modulus E, (b) hardness H, (c) change of film thickness δh, and (d) yield strength Y. The dashed lines show the location of the moving front. The shaded areas show the standard deviation. (For interpretation of the references to color in this figure legend, the reader is referred to the web version of this article.)

i.e., $0.33 \times \exp(-1)$, to the minimum value. Since the film is thin and the ion concentration is uniform in the through-thickness direction, the doping level is evaluated at the bottom of the film. The concentration and stress contours show little variation through the thickness direction of the film, here we take the values at the bottom of the model. As shown in Fig. 4(a) and the zoom-in view in (b), larger f_C for a steeper increase in diffusivity upon doping causes a sharper moving front. Table S1 lists the front width for different values of f_C. Among the tested range of f_C with a fixed value of $f_d = 1$, we select $f_C = 53$, which produces the closest value of the front width in experiments ($\sim$37 μm) and represents an increase of the diffusivity upon full doping by a factor of $\sim$300. In the future modeling, f_C remains fixed at 53. To match the apparent diffusivity estimated in Fig. 2(b), we now fit f_d such that the displacement of the moving front in the model matches that of the experiment. Here the propagation displacement of the front in the experiments is determined visually by the optical images as shown in Fig. 2(b), while in the modeling, we define the moving displacement to be the distance over which the doping level drops from its maximum value (0.33) to 36% of the maxima. In Fig. 4(c) and the zoom-in view (d), we plot the doping level at 1 h (solid line) and 2 h (dashed line) for $f_d = 1$ (cyan), $f_d = 2$ (gray), and $f_d = 3$ (magenta). Among the tested values, $f_d = 3$ gives a good agreement of the front displacement at the two times and is used in the modeling.

With the fitting parameters f_C, f_d at specific times, and the apparent diffusivity D_1 and D_2, we further validate the model and parameters in the long-time propagation of the moving front. Fig. 4(e) and Figure S3 shows that the front displacement predicted from the FEM for over 48 h agrees well with the experimental results. This corroborates the finding that the doping kinetics in the moving front experiment is a diffusion-controlled process. In Fig. 4(f), we plot the contours of the doping level, mean stress, and plastic strain at 48 h. The doped region holds a higher concentration of ions and thus a greater extent of volumetric swelling. Significant plastic deformation is observed to accommodate the swelling of PProDOT upon doping. The material yielding impacts the doping profile as the ion concentration profiles show kinks in Fig. 4(b) and (d). The kinks are formed due to the stress concentration at the moving front. Since the yield strength decreases with the doping level, the region where the yield condition is just reached has the largest compressive stress. The compressive stress increases the chemical potential of the mobile ions and drives diffusion from the compressed region to its vicinity. This raises the ion concentration ahead of the front and leads to kinks in ion distribution.

To further examine the impact of mechanical stresses on the doping kinetics, we conduct experiments on the moving front with an external pressure applied on the exposed surface of the film and observe the dynamic behavior. The setup is schematically shown in Fig. 5(a). The pressure is applied with a load-transmitting polyethylene terephthalate (PET) film under a steel plate wrapped with polyethylene (PE) to cover the sharp edges and prevent damage to the film during loading. Two office clamps are used to compress the stacked PProDOT thin film, load-transmitting plate, and pressure sensor. In the control experiment, the pressure sensor shows little decay before the release of the pressure after several days. We conduct experiments with increased pressure from 1.63 MPa to 12.31 MPa and observed that 2.80 MPa is a threshold of pressure to significantly retard the diffusion process, as shown in Figure S4. The camera photo and microscope image of the sample under a 2.80 MPa pressure are shown in Fig. 5(b). The region in direct contact with the electrolyte is completely bleached to transmissive light blue, and the moving front continues to propagate towards the un-doped domain. At $\sim$48 h, the front reaches the stressed region from the ion source. After an addition of $\sim$72 h, the test is terminated. For the pressured region, as seen in the camera photo and circled by the white dashed box in the microscope image in Fig. 5(b), a clear color contrast presents compared to the pressure-free region. The PProDOT film within the irregular regions outlined

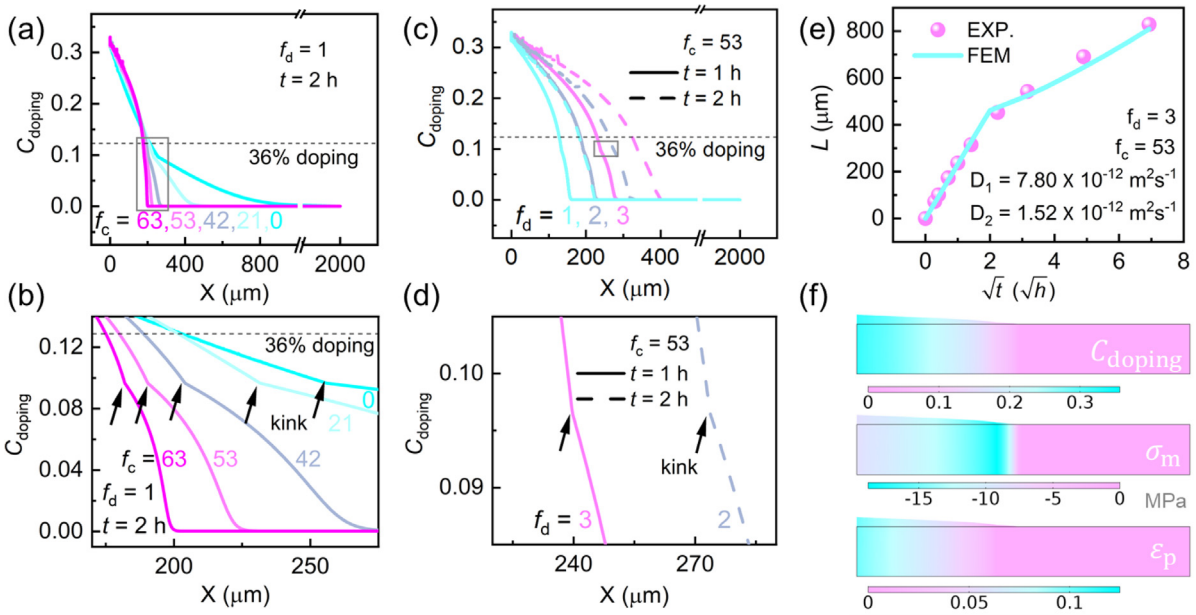

Fig. 4. Kinetics modeling of the moving front in PProDOT thin film. (a) Doping level profile for $f_C = 0, 21, 42, 53$, and 63 with $f_d = 1$. (b) Zoom-in view of the gray boxed region in (a). (c) Doping level profile for $f_d = 1, 2, 3$ with $f_C = 53$. (d) Zoom-in view of the gray boxed region in (c). (e) Front propagation displacement from experimental and FEM results plotted against the square root of time. (f) Contour plot of the doping level, mean stress, and plastic strain at 48 h. (For interpretation of the references to color in this figure legend, the reader is referred to the web version of this article.)

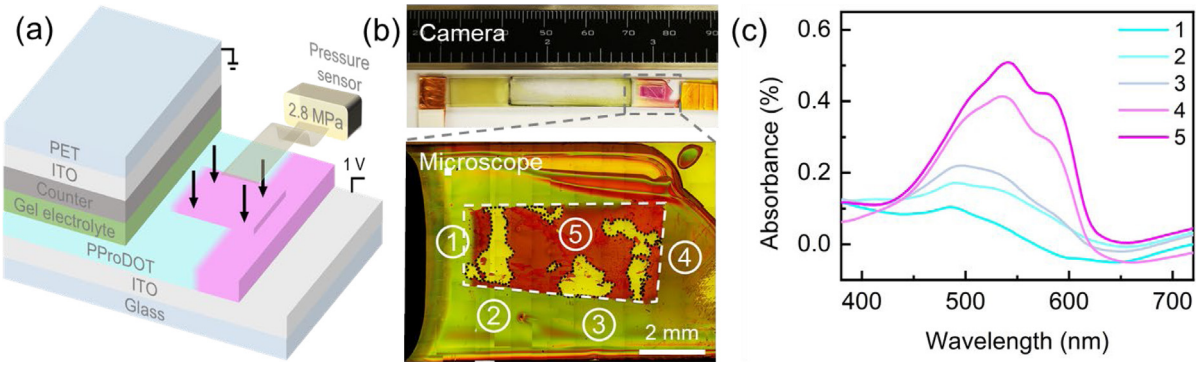

Fig. 5. Stress effect on the doping kinetics in the moving front experiment of PProDOT thin film. (a) Schematic of the setup with applied pressure (shown as vertical arrows) and a pressure sensor. (b) Camera photo and microscopic image of the sample showing the contrast between the doped region and un-doped region under stress. (c) Absolute absorbance across the visible spectrum for 5 locations labeled in (b). (For interpretation of the references to color in this figure legend, the reader is referred to the web version of this article.)

by the black dots is peeled off when the PET-PE plate is removed, leaving the bare ITO coated glass visible. We further employ UV–VIS spectroscopy to quantify the film absorbance at five different locations in the film, spanning across the pressured and stress-free regions, as shown in Fig. 5(c). The curves are adjusted such that the absorbance at 350 nm is approximately the same, since doping does not alter the ultraviolet spectrum of PProDOT [3]. The result shows that at locations 1, 2, and 3, where the color is light, the absorbance is low or intermediate, implying that the moving front has passed through. In contrast, in the pressured region 5, the absorbance is very high, on par with the absorbance of pristine PProDOT magenta films. This indicates that the mobile ions have not yet reached the region in magenta and the doping process did not start. Region 4 has the second highest absorbance among all. Figure S5 shows the current in the PProDOT film as a function of time after the moving front reaches the stressed region. The current density starts increasing after ~60 h, indicating a higher ion consumption rate at the moving front and thus an increased current density. The decreased absorbance in region 4 compared to region 5 and the increased current density in Figure S5 indicate that the moving front reaches beyond the stressed region. The front propagation displacement of the stress-free region is ~6.21 mm whereas in the stressed region it is ~0.40 mm for 72 h, showing that the stress impacts the diffusivity roughly by a factor of $\frac{D}{D_s} = \left(\frac{L}{L_s}\right)^2 = \left(\frac{6.21}{0.40}\right)^2 = 241$. As discussed before, the doping level can alter the ionic diffusivity by ~300 times. The mechanical stress has a comparable impact on the ionic transport as that by electrochemical doping.

To understand the effect of mechanical stresses on the doping kinetics, we use finite element analysis to evaluate the role of stress in the following four conditions: (i) control condition (Ctrl) without applied pressure and $f_s = 0$, (ii) pressured condition (P) with an applied pressure and $f_s = 0$, (iii) stressed condition (f_s) without applied pressure and $f_s = 6$, and (iv) combined condition (P&f_s) with an applied pressure and $f_s = 6$. Compared to the control, the other three conditions show their influence on the doping kinetics due to the stress effect on

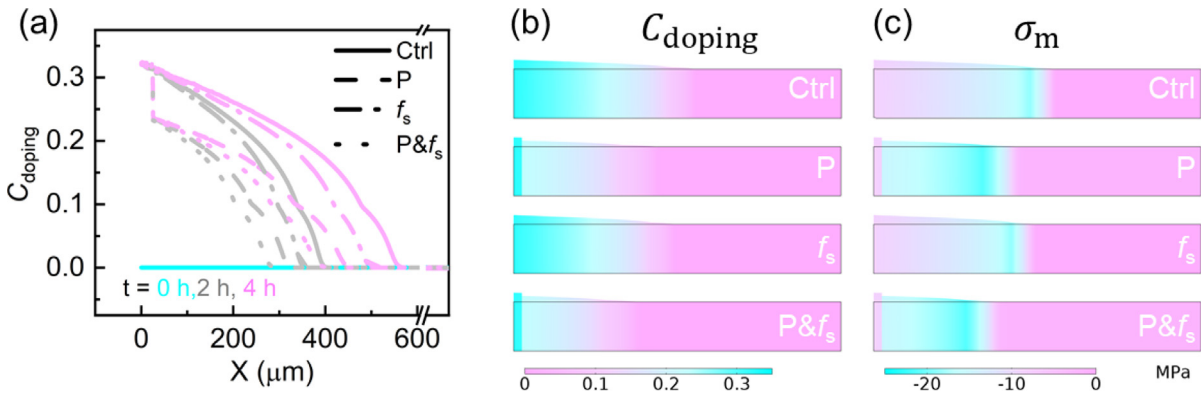

Fig. 6. Finite element modeling results on stress effect on doping kinetics in PProDOT thin film. (a) Doping level profile at the bottom of the thin film model for 4 conditions. Colors of cyan (0 h), gray (2 h), and magenta (4 h) show doping levels at different times. (b) Doping level contour and (c) mean stress contour for the four conditions at 4 h. (For interpretation of the references to color in this figure legend, the reader is referred to the web version of this article.)

chemical potential (pressured condition P), the stress effect on ionic diffusivity (stressed condition f_s), and combined effects on chemical potential and diffusivity (P&f_s). Fig. 6 shows the doping level profile and contour, and the mean stress contour for the four conditions. In Fig. 6(a), different conditions are represented by different lines (solid, dashed, dash-dotted, dotted). For the same condition, colors of cyan (0 h), gray (2 h), and magenta (4 h) represent the doping level at different times. In the control condition (solid line in Fig. 6(a)), the front velocity is the highest. Under the pressured condition (dashed line) the film experiences higher compressive stresses compared to the control condition. The applied pressure induces a large stress gradient across the boundary of the pressured region, which in turn leads to a large gradient in the chemical potential of the mobile ions. Therefore, the pressured region accepts fewer ions from the doped pressure-free region, leading to a drastic drop in concentration at the edge of the pressured region. Compared to the control condition, the stressed condition (dash-dotted line) unveils the effect of the self-generated stress on diffusivity upon doping. The ion insertion-induced swelling of the film is under constraint by the substrate. The induced compressive stress contribute to the term $\exp\left(f_s \frac{\sigma_m}{G}\right)$ in the diffusivity. Here, the front propagation is also slowed, but faster than the condition P. Lastly, for the combined condition (dotted line), a drastic drop in the doping level is shown at the boundary of the pressured region and results in the slowest front velocity.

From the results we see that both the self-generated stress and the applied pressure have a significant influence on the doping reaction. Both increase the magnitude of the mean stress σ_m. The effect of the mean stress on doping process is twofold. Thermodynamically, the mean stress contributes to the chemical potential of the mobile species. A large compressive mean stress increases the chemical potential. Thus, the driving force for ions to diffuse into the pressured region is decreased. Kinetically, the mean stress contributes to the term exp $\left(f_s \frac{\sigma_m}{G}\right)$ in the apparent diffusivity. A large compressive mean stress decreases the apparent diffusivity, which slows down ion diffusion in the pressured region. Both factors tend to retard the doping reaction under the pressured region.

For the four conditions, we back-calculate the apparent diffusivity from the front propagation displacement. For the control, P, f_s, and P&f_s conditions, the apparent diffusivities calculated by $D = \frac{L^2}{2t}$ are 7.41×10^{-12} m^2 s^{-1}, 3.39×10^{-12} m^2 s^{-1}, 5.69×10^{-12} m^2 s^{-1}, and 2.42×10^{-12} m^2 s^{-1}, respectively. The drastic change in doping level, mean stress, and thickness are further evident in Figs. 6(b) and (c). Compared to the previously estimated $\frac{D}{D_s} = 241$ from experiments, here the modeling results seem to underestimate the stress effect on the doping kinetics. The reasons for the discrepancy may be that (i) we used a lower limit for stress factor f_s in the literature and (ii) the front propagation time in the FEM simulation is 4 h given the high computational cost, which is much shorter than that in the experiments. Nevertheless, the theory and modeling results have demonstrated the significance of stress on the doping kinetics in OMIECs.

3. Conclusion

In conclusion, we reveal the doping kinetics of a model organic mixed ionic–electronic conductor, PProDOT, using the combined moving front experiments and theoretical modeling. The bilinear relationship between the moving front displacement and the square root of time shows the diffusion characteristic of the doping process. The experimental setup allows in-situ measurement of the mechanical properties and swelling of the thin film upon doping. We also identify that an externally applied pressure of 2.8 MPa significantly retards the ion transport and the doping process. We employ theoretical modeling and finite element analysis to evaluate the dependence of ionic diffusivity on the doping level and mechanical stress. Results show that the self-generated compressive stress in the film due to the redox reaction and the externally applied pressure both slow the doping kinetics. Our work presents a fundamental understanding of the coupled electrochemical and mechanical responses of OMIECs in their solid-state devices.

4. Methods

Device fabrication: PProDOT was synthesized via direct arylation polymerization [46]. The number average molecular weight is ∼11.1 kDa, with polydispersity index of 1.3. The powders were dissolved in chloroform (20 mg mL^{-1}) and stirred overnight to form a homogeneous solution before use. ITO-coated glass slides were cleaned with ultrasonic in chloroform and then ethanol for 10 min. The PProDOT solution was then spin-coated on ITO-coated glass slides with a spin speed of 1500 rpm to form films of the thickness of ∼100 nm. The absorbance spectra were characterized by UV–Vis–NIR spectrometer Cary-5000. The film thickness was measured by the indentation test described in our previous work [9]. VO_x counter electrodes were synthesized, spin-coated, and annealed as described in detail in our previous work (with a thickness of about 200 nm) [20]. Gel electrolyte was photocured for 10 min using the precursor with 5:5:1 volume ratio of 1 M LiTFSI/PC, poly(ethylene glycol) methyl ether acrylate

(M_n = 480, Sigma Aldrich), and photoinitiator 2-hydroxy-2-methylpropiophenone (Sigma Aldrich).

In-situ nanoindentation: In-situ nanoindentation experiments were done using the Agilent G200 indenter. Film thickness was measured by scratch test embedded in the Nano Suite software. Continuous stiffness measurement with the substrate calibration method was utilized for modulus and hardness test. Thermal drift and airflow are minimized since the indenter is located inside the Ar-filled glovebox. The device is powered by VersaStat Potentiostat 3 (Princeton Applied Research) with a fixed voltage of 1 V. The indentation is performed with the applied voltage when the moving front propagates over ∼1 mm. Optical images are taken during the experiments.

Theory: We formulate the coupled diffusion and large deformation theory within the continuum mechanics framework. Consider a material point $\boldsymbol{X}$ in the reference state and $\boldsymbol{x}$ in the current state. The deformation gradient is decomposed into three parts $\boldsymbol{F} = \frac{\partial \boldsymbol{x}}{\partial \boldsymbol{X}} = \boldsymbol{F}_{\text{el}}\boldsymbol{F}_{\text{inel}} = \boldsymbol{F}_{\text{el}}\boldsymbol{F}_{\text{C}}\boldsymbol{F}_{\text{pl}}$, i.e., the elastic contribution $\boldsymbol{F}_{\text{el}}$, the ion insertion induced $\boldsymbol{F}_{\text{C}} = (1 + C\Omega)^{1/3}$, and the plastic portion $\boldsymbol{F}_{\text{pl}}$. C is the ion concentration and Ω is the partial molar volume. $\boldsymbol{\varepsilon} = \left(\boldsymbol{F}^{\text{T}}\boldsymbol{F} - \boldsymbol{I}\right)/2$ is the total strain. Denote that $J = \det(\boldsymbol{F})$. Cauchy stress tensor $\boldsymbol{\sigma} = J^{-1}\boldsymbol{F}\boldsymbol{S}\boldsymbol{F}^{\text{T}}$ is derived from the 2nd Piola–Kirchhoff stress tensor $\boldsymbol{S} = J_{\text{C}}\boldsymbol{F}_{\text{inel}}^{-1}\frac{\partial W(\boldsymbol{F},C)}{\partial \boldsymbol{\varepsilon}}\boldsymbol{F}_{\text{inel}}^{-\text{T}}$, which is partial derivatives of the free energy function density $W(\boldsymbol{F}, C)$. Finally, we solve the equilibrium equation $\nabla\cdot(\boldsymbol{F}\boldsymbol{S}) = \boldsymbol{0}$. The Neo-Hookean constitutive relation is chosen, and the free density function is $W_{\text{e}} = \frac{1}{2}G(I_1 - 3) - G\ln(J_{\text{el}}) + \frac{1}{2}\lambda[\ln(J_{\text{el}})]^2$, where G is the shear modulus, λ the Lamé parameter, and I_1 the first invariant of the right Cauchy–Green deformation tensor. Von Mises yield criterion is adopted for the plastic deformation and the yield function is $F_{\text{y}} = \sigma_{\text{mises}} - Y = \sqrt{\frac{3}{2}\boldsymbol{\sigma}_{\text{d}}:\boldsymbol{\sigma}_{\text{d}}} - Y$, where $\boldsymbol{\sigma}_{\text{d}}$ the deviatoric stress. The plastic rule follows that $\dot{\boldsymbol{C}}_{\text{pl}}^{-1} = -\frac{2\Lambda}{J}\boldsymbol{F}^{-1}\frac{\partial F_{\text{y}}}{\partial \boldsymbol{\sigma}}\boldsymbol{F}\boldsymbol{C}_{\text{pl}}^{-1}$, where $\boldsymbol{C}_{\text{pl}} = \boldsymbol{F}_{\text{pl}}^{\text{T}}\boldsymbol{F}_{\text{pl}}$. The yield function F_{y} and the plastic multiplier Λ fulfill the Kuhn–Tucker conditions: [47] $\Lambda \geq 0$, $F_{\text{y}} \leq 0$, and $\Lambda F_{\text{y}} = 0$. The total free energy density function $W = W_{\text{e}} + W_{\text{C}}$, and W_{C} defines the chemical potential of the mobile ions $\mu = \frac{\partial W(\boldsymbol{F},C)}{\partial C} = \mu_0 + RTln\left(\frac{C}{C_{\max}-C}\right) - \sigma_{\text{m}}\Omega = \mu_0 + RTln\left(\frac{C_{\text{doping}}}{1-C_{\text{doping}}}\right) - \sigma_{\text{m}}\Omega$, where μ_0 is the reference chemical potential, R is the gas constant, T is the temperature, and σ_{m} is the mean stress. The flux is defined proportional to the gradient of the chemical potential, $\boldsymbol{J} = -\frac{CD}{RT}\boldsymbol{F}^{-1}\boldsymbol{F}^{-\text{T}}\nabla\mu$, where D is the diffusivity. Finally, the continuity equation is solved, $\dot{C} + \nabla\cdot\boldsymbol{J} = 0$.

Finite element modeling: COMSOL Multiphysics 5.5 is used for the implementation of the theory. A thin film geometry of 1 mm by 100 nm is built to resemble the cross-section of the film, as shown in Figure S6. The bottom of the film is fixed, while the left/right ends are with roller constraints. For the diffusion model, the left (right) boundary is set to the maximum (minimum) concentration with the initial concentration set as the minimum globally. The material parameters are listed in Table S2. The tangent modulus during strain hardening is set as 1% of the modulus for convergence. The mesh sensitivity is checked. Due to the computational cost, we assume in the model that the expansion of the film due to ion insertion is 20% which is smaller than the experimental data of 34%. This choice should have little impact on the results because most of the deformation of the thin film is beyond the elastic limit and is accommodated by plastic flow which does not incur further growth of stress.

Declaration of competing interest

The authors declare the following financial interests/personal relationships which may be considered as potential competing interests: J. M. is a co-founder of Ambilight Inc.

Acknowledgments

K. Z. and X. W. acknowledge the support of the School of Mechanical Engineering at Purdue University. The authors appreciate the help from Dr. Liyan You at Purdue University for the synthesis of the PProDOT material.

Appendix A. Supplementary data

Supplementary material related to this article can be found online at https://doi.org/10.1016/j.eml.2022.101739.

References

[1] J. Rivnay, S. Inal, A. Salleo, R.M. Owens, M. Berggren, G.G. Malliaras, Nat. Rev. Mater. 3 (2018) 1.
[2] E. Zeglio, O. Inganäs, Adv. Mater. 30 (2018) 1800941.
[3] X. Li, K. Perera, J. He, A. Gumyusenge, J. Mei, J. Mater. Chem. C 7 (2019) 12761.
[4] X. Li, X. Chen, Z. Jin, P. Li, D. Xiao, Mater. Chem. Front. 5 (2021) 1140.
[5] E. Fresta, R.D. Costa, Adv. Funct. Mater. 30 (2020) 1908176.
[6] B.D. Paulsen, K. Tybrandt, E. Stavrinidou, J. Rivnay, Nature Mater. 19 (2020) 13.
[7] A.D. Scaccabarozzi, A. Basu, F. Aniés, J. Liu, O. Zapata-Arteaga, R. Warren, Y. Firdaus, M.I. Nugraha, Y. Lin, M. Campoy-Quiles, N. Koch, C. Müller, L. Tsetseris, M. Heeney, T.D. Anthopoulos, Chem. Rev. (2021).
[8] C.M. Amb, A.L. Dyer, J.R. Reynolds, Chem. Mater. 23 (2011) 397.
[9] X. Wang, K. Chen, L.S. de Vasconcelos, J. He, Y.C. Shin, J. Mei, K. Zhao, Nature Commun. 11 (2020) 211.
[10] X. Wang, L.S. de Vasconcelos, K. Chen, K. Perera, J. Mei, K. Zhao, ACS Appl. Mater. Interfaces 12 (2020) 50889.
[11] L.Q. Flagg, R. Giridharagopal, J. Guo, D.S. Ginger, Chem. Mater. 30 (2018) 5380.
[12] T.J. Quill, G. LeCroy, A. Melianas, D. Rawlings, Q. Thiburce, R. Sheelamanthula, C. Cheng, Y. Tuchman, S.T. Keene, I. McCulloch, R.A. Segalman, M.L. Chabinyc, A. Salleo, Adv. Funct. Mater. 31 (2021) 2104301.
[13] B.D. Paulsen, R. Wu, C.J. Takacs, H.-G. Steinrück, J. Strzalka, Q. Zhang, M.F. Toney, J. Rivnay, Adv. Mater. 32 (2020) 2003404.
[14] L.Q. Flagg, C.G. Bischak, J.W. Onorato, R.B. Rashid, C.K. Luscombe, D.S. Ginger, J. Am. Chem. Soc. 141 (2019) 4345.
[15] G. Rebetez, O. Bardagot, J. Affolter, J. Réhault, N. Banerji, Adv. Funct. Mater. (2021) 2105821.
[16] C. Odin, M. Nechtschein, Synth. Met. 55 (1993) 1281.
[17] K. Zhang, Y. Xie, B.B. Noble, M.J. Monteiro, J.L. Lutkenhaus, K. Oyaizu, Z. Jia, J. Mater. Chem. A 9 (2021) 13071.
[18] A. Savva, C. Cendra, A. Giugni, B. Torre, J. Surgailis, D. Ohayon, A. Giovannitti, I. McCulloch, E. Di Fabrizio, A. Salleo, J. Rivnay, S. Inal, Chem. Mater. 31 (2019) 927.
[19] N. Delavari, J. Gladisch, I. Petsagkourakis, X. Liu, M. Modarresi, M. Fahlman, E. Stavrinidou, M. Linares, I. Zozoulenko, Macromolecules 54 (2021) 6552.
[20] X. Li, Z. Wang, K. Chen, D.Y. Zemlyanov, L. You, J. Mei, ACS Appl. Mater. Interfaces 13 (2021) 5312.
[21] S.E. Feicht, G.D. Degen, A.S. Khair, AIChE J. 61 (2015) 1447.
[22] J. Rivnay, S. Inal, B.A. Collins, M. Sessolo, E. Stavrinidou, X. Strakosas, C. Tassone, D.M. Delongchamp, G.G. Malliaras, Nature Commun. 7 (2016) 11287.
[23] M. Berggren, G.G. Malliaras, Science 364 (2019) 233.
[24] E. Stavrinidou, P. Leleux, H. Rajaona, D. Khodagholy, J. Rivnay, M. Lindau, S. Sanaur, G.G. Malliaras, Adv. Mater. 25 (2013) 4488.
[25] E. Stavrinidou, P. Leleux, H. Rajaona, M. Fiocchi, S. Sanaur, G.G. Malliaras, J. Appl. Phys. 113 (2013) 244501.
[26] J.C. Lacroix, K. Fraoua, P.C. Lacaze, J. Electroanal. Chem. 444 (1998) 83.
[27] X. Wang, E. Smela, J. Phys. Chem. C 113 (2009) 369.
[28] H.W. Heuer, R. Wehrmann, S. Kirchmeyer, Adv. Funct. Mater. 12 (2002) 89.
[29] T. Deutschmann, E. Oesterschulze, J. Opt. 16 (2014) 075301.
[30] S. Sen, S.Y. Kim, L.R. Palmore, S. Jin, N. Jadhav, E. Chason, G.T.R. Palmore, ACS Appl. Mater. Interfaces 8 (2016) 24168.
[31] R. Blau, AX. Chen, B. Polat, LL. Becerra, R. Runser, B. Zamanimeymian, K. Choudhary, DJ. Lipomi, ACS Appl. Mater. Interfaces (2022) http://dx.doi.org/10.1021/acsami.1c18495.
[32] H. Okuzaki, H. Suzuki, TJ. Ito, Synth. Met. 159 (2009) 21–22.
[33] L.S. de Vasconcelos, R. Xu, K. Zhao, J. Mech. Phys. Solids 144 (2020) 104102.
[34] H. Mehrer, Defect Diffus. Forum 129–130 (1996) 57.
[35] X. Li, X. Wang, L. You, K. Zhao, J. Mei, ACS Mater. Lett. 7 (2022) 4.

[36] B.S. Bokstein, M.I. Mendelev, D.J. Srolovitz, Thermodynamics and Kinetics in Materials Science: A Short Course, Oxford University Press, Incorporated, Oxford, UNITED KINGDOM, 2005.
[37] T. Deutschmann, C. Kortz, L. Walder, E. Oesterschulze, Opt. Express OE 23 (2015) 31544.
[38] D.M. Marsh, A.H. Cottrell, Proc. R. Soc. Lond. Ser. A Math. Phys. Eng. Sci. 279 (1964) 420.
[39] K.L. Johnson, J. Mech. Phys. Solids 18 (1970) 2.
[40] K.W. McElhaney, J.J. Vlassak, W.D. Nix, J. Mater. Res. 13 (1998) 1300.
[41] D. Kim, I. Zozoulenko, J. Phys. Chem. B 123 (2019) 5160.
[42] P. Das, B. Zayat, Q. Wei, C.Z. Salamat, I.-B. Magdău, R. Elizalde-Segovia, D. Rawlings, D. Lee, G. Pace, A. Irshad, L. Ye, A. Schmitt, R.A. Segalman, T.F. Miller, S.H. Tolbert, B.S. Dunn, S.R. Narayan, B.C. Thompson, Chem. Mater. 32 (2020) 9176.
[43] A.A. Fahmy, J.C. Hurt, Polym. Compos. 1 (1980) 77.
[44] S. Neumann, G. Marom, Polym. Compos. 6 (1985) 9.
[45] G. Youssef, S. Fréour, F. Jacquemin, J. Compos. Mater. 43 (2009) 1621.
[46] L.A. Estrada, J.J. Deininger, G.D. Kamenov, J.R. Reynolds, ACS Macro Lett. 2 (2013) 869.
[47] J. Lubliner, Plasticity Theory, Courier Corporation, 2008.